*Nano Research* 2017, 10(3): 922–932
DOI 10.1007/s12274-016-1350-0
**Research Article**
ISSN 1998-0124
CN 11-5974/O4

# Heterogeneous synergistic catalysis by Ru-$RuO_x$ nanoparticles for Se–Se bond activation

Mu Lin[1], Liqun Kang[1], Jun Gu[1], Linxiu Dai[1], Shengbo Tang[1], Tao Zhang[1], Yuhao Wang[1], Lindong Li[1], Xiaoyu Zheng[1], Wei Zhu[1], Rui Si[2], Xuefeng Fu[1], Lingdong Sun[1] (✉), Yawen Zhang[1] (✉), and Chunhua Yan[1] (✉)

[1] *Beijing National Laboratory for Molecular Sciences, State Key Laboratory of Rare Earth Materials Chemistry and Applications, PKU-HKU Joint Laboratory in Rare Earth Materials and Bioinorganic Chemistry, College of Chemistry and Molecular Engineering, Peking University, Beijing 100871, China*

[2] *Shanghai Synchrotron Radiation Facility, Shanghai Institute of Applied Physics, Chinese Academy of Sciences, Shanghai 201204, China*

**Received:** 20 September 2016
**Revised:** 28 October 2016
**Accepted:** 29 October 2016



**KEYWORDS**
nanoparticle,
ruthenium,
selenium,
heterogeneous catalysis,
synergistic effect

## ABSTRACT

The transition from homogeneous to heterogeneous synthetic chemistry enabled by nanocatalysts necessitates investigations of the reaction mechanism and structure-activity relationships for inorganic nanoparticles and organic substrates. Herein, we report that hydrothermally synthesized ruthenium nanoparticles performed differently in the Se–Se bond activation and selenylation of heterocycles, exhibiting a volcano-shaped relationship between catalytic activity and composition. A synergistic effect was observed for Ru-$RuO_x$ nanocatalysts, with numerous characterizations and density functional theory (DFT) calculations suggesting that a PhSeSePh molecule can initially be adsorbed on the metallic Ru sites and cleaved into two PhSe* species, which subsequently migrate to $RuO_x$ sites and react with the nucleophile to achieve the selenylation of heterocycles.

## 1 Introduction

The development of green chemistry has made nanocatalysis a new frontier, bridging homogeneous and heterogeneous catalytic processes and uniting their advantages. The large nanoparticle surface area leads to enhanced contact between the catalyst and the reactants, and the insolubility of these nanocatalysts in the reaction medium enables their convenient separation [1–18]. Compared to homogeneous catalysts, studies on nanocatalysts are still in the preliminary stage, owing to the more complex structures and complicated structure-activity relationships involved. Various factors including size, shape, exposed surface, oxidation level, and structure of the nanocatalysts may significantly influence their catalytic properties. Thus, to develop novel nanocatalysts with high activities, a deep understanding of the related catalytic mechanism

Address correspondence to Chunhua Yan, yan@pku.edu.cn; Yawen Zhang, ywzhang@pku.edu.cn; Lingdong Sun, sun@pku.edu.cn

and structure-activity relationships is required.

The activation of chalcogen–chalcogen bonds is of great significance in chemistry, as the formation of carbon–chalcogen bonds can produce numerous biologically active compounds and organic materials. In particular, Se–Se bond activation and C–Se bond formation are vital for biological systems, being widely applied in industrial catalysis, organic electronics, and the fabrication of semiconductors and nanomaterials [19–21]. The still challenging synthesis of ideal catalysts for these processes is thus of great interest. Dinuclear Ru complexes are common catalysts for activating Se–Se bonds via the oxidative addition of diaryl diselenides on two metal site (Scheme S1 in the Electronic Supplementary Material (ESM)) [22–30]. However, dinuclear catalysts are usually synthesized and stabilized using complex ligands, which is challenging. Moreover, the produced dinuclear Ru metallacycles are often stable, hindering the following C–Se bond formation step to afford the product. Thus, Ru nanoparticles with multiple Ru centers on their surface are considered suitable candidates for catalyzing Se–Se bond activation.

Herein, we report that Ru nanospheres (NSs) support the Se–Se bond activation and selenylation of heterocycles under ambient conditions, with their catalytic activities related to the synergistic effect of metallic Ru and $RuO_x$. Based on the results of systematic characterization and DFT calculations, a plausible mechanism is proposed.

## 2 Experimental

### 2.1 Materials

$RuCl_3{\cdot}xH_2O$ (A.R., Sinopharm Chemical Reagent Co., Ltd.), sodium malonate ($Na_2C_3H_2O_4{\cdot}H_2O$, A.R., Beijing Chemical Works), polyvinylpyrrolidone (PVP; $M_W$ ~ 29,000, Sigma-Aldrich), formaldehyde solution (HCHO, 40 wt.%, A.R., Beijing Yili Fine Chemical Reagent Corp.), and acetone (A.R.) were used as received. Ultrapure water was used in all experiments (Millipore, 18.2 MΩ).

### 2.2 Preparation of Ru nanospheres

#### 2.2.1 *Hydrothermal synthesis of Ru nanospheres*

In a typical synthesis, PVP (100 mg, $M_W$ ~ 29,000) and $Na_2C_3H_2O_4{\cdot}H_2O$ (140 mg) were dissolved in ultrapure water (10 mL), followed by the addition of $RuCl_3{\cdot}xH_2O$ (0.24 mmol) and formaldehyde (400 μL, 40 wt.%). The reaction mixture was diluted to 15 mL, loaded in a 25-mL Teflon-lined container, and sealed in a matched steel autoclave. The autoclave was subsequently heated in an oven at 160 ℃ for 8 h. After the reaction, the autoclave was allowed to cool to room temperature, and acetone (45 mL) was added. The product was collected by centrifugation at 7,800 rpm for 10 min. The precipitate was washed by a water/acetone (1:3 v/v) mixture for three times, and the product (denoted as Ru-NSs-1), was dispersed in methanol by ultrasonication. The yield of Ru nanospheres was determined as ~90% by inductively coupled plasma atomic emission spectroscopy (ICP-AES) analysis.

#### 2.2.2 *Hydrothermal oxidation/reduction of Ru nanospheres*

The as-synthesized Ru-NSs-1 were post-reduced by hydrogen under hydrothermal conditions for 1, 4, and 12 h (denoted as Ru-NSs-2, Ru-NSs-3, and Ru-NSs-4, respectively) and post-oxidized by oxygen for 1 and 4 h (denoted as Ru-NSs-5 and Ru-NSs-6, respectively). The reduction process generating Ru-NSs-2 was used to adjust and regulate the surface composition of Ru-NSs-1. The as-obtained Ru-NSs-1 was dispersed in water (15 mL) containing PVP (100 mg), and the dispersion was loaded into a 50-mL Teflon-lined reactor subsequently filled with $H_2$ to a pressure of 2.0 MPa. The reduction was performed at 150 ℃ for 1 h. After the reaction, acetone (45 mL) was added, and the Ru nanospheres were collected by centrifugation at 7,800 rpm for 10 min. A similar process was used to obtain Ru-NSs-3 (2.0 MPa of $H_2$, 150 ℃ for 4 h), Ru-NSs-4 (2.0 MPa of $H_2$, 150 ℃ for 12 h), Ru-NSs-5 (2.0 MPa of $O_2$, 150 ℃ for 1 h), and Ru-NSs-6 (2.0 MPa of $O_2$, 150 ℃ for 4 h).

### 2.3 Characterization

Samples for transmission electron microscopy (TEM) imaging were prepared by drying a drop of an ethanolic dispersion of the samples on copper grids coated with amorphous carbon membranes. TEM and high-resolution TEM (HRTEM) images were recorded on a FEG-TEM instrument (JEM2100F, JEOL, Japan) operated at 200 kV. More than 100 particles

were sampled to calculate the average size of Ru nanospheres for each sample. X-ray diffraction (XRD) patterns were recorded on an X'Pert Pro diffractometer (PANalytical B.V., the Netherlands) at a scanning rate of 1 °·min$^{-1}$ using Cu K$\alpha$ radiation, with the K$\alpha_2$ line contributions in the XRD patterns subtracted. X-ray photoelectron spectroscopy (XPS) characterization was performed on an Axis Ultra spectrometer (Kratos Analytical Ltd., Japan). The content of Ru in different oxidation states was determined by fitting the high-resolution Ru 3d XPS spectra in the range of 270–295 eV. The concentration of the Ru nanosphere dispersion was determined by ICP-AES. A 50-μL aliquot of the dispersion was initially transferred into a 25-mL Teflon-lined container and dried. Hydrochloric acid (4 mL) and nitric acid (0.05 mL) were added, and the container was sealed in a matched steel autoclave and transferred into an oven kept at 180 °C. The autoclave was removed after 12 h and cooled to room temperature. The yellow solution was diluted to 10.0 mL and used for ICP-AES analysis, which was performed on a Profile Spec ICP-AES spectrometer (Leeman, USA). Ru K-edge and Se K-edge X-ray absorption fine structure (XAFS) analyses were performed in transmission mode on the BL14W1 beamline of the Shanghai Synchrotron Radiation Facility (SSRF) and on the 1W1 XAFS beamline of the Beijing Synchrotron Radiation Facility (BSRF).

### 2.4 Se–Se bond activation for the selenylation of heterocycles catalyzed by Ru nanocatalysts

The reactions were stirred using Teflon-coated magnetic bars. Elevated temperatures were maintained using thermostat-controlled silicone oil baths. Organic solutions were concentrated using a Büchi rotary evaporator with a desktop vacuum pump. Chemicals were purchased from Acros, Aldrich, Alfa Aesar, Beijing Chemical Works, and Beijing Yili Fine Chemical Reagent Corp. and were used without further purification, unless otherwise indicated. Analytical TLC was performed using 0.25-mm silica gel G plates with a 254-nm fluorescent indicator. The TLC plates were visualized by ultraviolet light and phosphomolybdic acid staining followed by gentle heating. Product purification was accomplished by flash chromatography on silica gel, and the purified compounds showed a single spot in analytical TLCs.

The concentrations of colloidal methanolic solutions of Ru nanoparticles were determined by ICP-AES. The concentration of Ru-NSs-1 (5.61 mg·mL$^{-1}$, 8 mol.%) was calculated in accordance with the Ru atomic mass. The catalyst was dissolved in the solvent mixture ($H_2O$/$CH_3OH$, 1:1 v/v) together with 1 equiv. of indoles and 2–3 equiv. of selenide derivatives. The mixture (0.10 M concentration) was stirred for 96 h at room temperature, and the reaction tube was also immersed under room temperature. When TLC analysis indicated the disappearance of the starting material, the reaction mixture was filtered through a thin pad of silica gel. The filter cake was washed with petroleum ether (PE)/ethyl acetate (EA), and the combined filtrate was concentrated. The crude product was purified by flash column chromatography on silica gel.

## 3 Results and discussion

Ru nanocatalysts were prepared using a hydrothermal strategy [31]. In this method, $RuCl_3$ (0.24 mmol) was reduced by formaldehyde (400 μL, 40 wt.%) in the presence of PVP at 160 °C. $Na_2C_3H_2O_4{\cdot}H_2O$ was introduced to strongly coordinate with $Ru^{3+}$ ions and retard their reduction. The obtained Ru NSs (denoted as Ru-NSs-1), as revealed by the TEM images shown in Figs. 1(a) and 1(b), were poorly crystalline particles with an average diameter of 3.1 ± 0.3 nm and a specific surface area of 159 m$^2$·g$^{-1}$. Their XRD pattern (Fig. S2 in the ESM) shows no diffraction peaks of Ru oxides, such as $RuO_2$. Ru-NSs-1 was then used to activate the Se–Se bond of diphenyl diselenide (PhSeSePh), achieving the selenylation of indole [32–35] in high yields (up to 99%, entry 1, Table 2). The catalytic behavior of Ru NSs after recycling was also examined, with only slight changes in the yield of the gram-scale reaction observed (Fig. 1(c), 93% yield for the freshly prepared Ru NSs, with 89%, 92%, 90%, 88%, and 84% yields obtained for recycled NSs).

To determine the nature of the investigated catalytic processes, one needs to test if the Ru ions can leach from the nanoparticles into the reaction system. Otherwise, it would be difficult to determine if the reactions correspond to heterogeneous or homogeneous catalysis, since the leached metal ions might also be

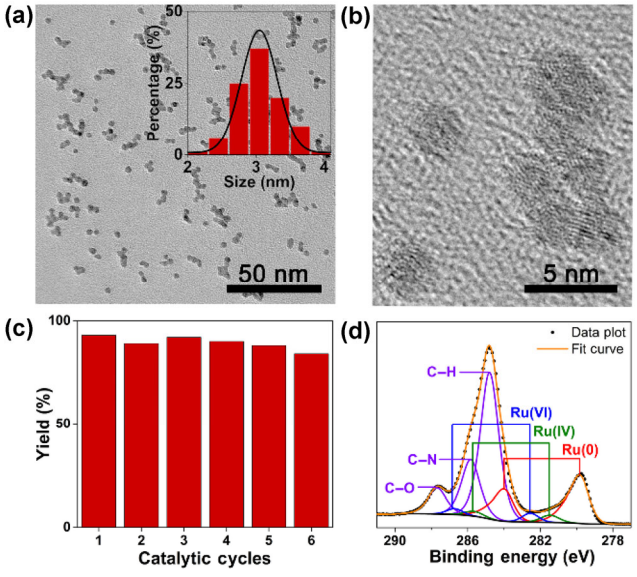


**Figure 1** (a) TEM image with a size distribution chart and (b) HRTEM image of Ru-NSs-1. (c) Recycling capability of Ru NSs according to the yields of **3a**. (d) C 1s and Ru 3d XPS spectra of Ru-NSs-1, deconvoluted into three C 1*s* peaks (violet curves) at 284.80, 285.80, and 287.63 eV, assigned to C atoms in C–H, C–N, and C=O moieties, respectively, and into Ru 3d doublets ($3d_{5/2}$ and $3d_{3/2}$, $\Delta$ = 4.17 eV) with Ru $3d_{5/2}$ binding energies of 279.5–279.9, 281.2–281.4, and 282.6–282.8 eV, assigned to Ru(0) (red curves), Ru(IV) (green curves), and Ru(VI) (blue curves) states, respectively [36, 37]. All results of the Ru 3d XPS spectra fitting are listed in Table S2 (in the ESM).

catalytically active. Therefore, after the reaction was complete, the Ru NSs were removed from the mixture, and the remaining solution was examined by ICP-AES. No Ru was detected in the organic or water phases, and the TEM images (Fig. S3 in the ESM), XPS spectra (Figs. 2(a) and 2(b)), and R-space EXAFS spectra (Fig. 2(c)) of the recycled Ru-NSs showed no significant difference from Ru-NSs-1 in the morphology and oxidation level. These results indicate that the Ru nanocatalysts remained stable during the reaction. Furthermore, the solution recovered after removing Ru NSs was unable to catalyze the model reaction. Thus, it was concluded that Ru NSs did not leach to form a homogeneous active catalyst in this catalytic system.

To investigate the origin of the superior catalytic activity of Ru NSs, an *in situ* XAFS analysis of Ru NSs was performed, using the model reaction of PhSeSePh with indole catalyzed by Ru-NSs-1 at 70 °C. The Fourier transform (FT) of the $k^2$-weighted extended X-ray adsorption fine structure (EXAFS) data obtained for Ru NSs in the reaction system showed peaks at 2.42, 2.67, and 1.96 Å, attributed to Ru–Se, Ru–Ru, and Ru–O scattering, respectively (Fig. 3(a), and Fig. S5 and Table S3 in the ESM) [38]. The XPS spectra in Fig. 1(d) also show that the surface of Ru-NSs-1 contained both metallic and oxidized Ru (denoted as Ru-$RuO_x$). Notably, when Ru NSs were exposed to the reaction system for 10 h, the peak intensity of Ru–Se scattering (2.42 Å) [24, 27, 39–42] was initially significantly increased. The subsequent intensity decrease indicated the *in situ* formation of Ru–Se bonds on the surface of Ru NSs followed by their cleavage (Fig. 3(b) and Table S3 in the ESM), related to the Se–Se bond activation and selenylation of heterocycles in the catalytic reaction.

Based on Ru-$RuO_x$ nanocatalysts and the organocatalytic process, DFT calculations were also carried out to understand the relationship between the surface composition and catalytic activity (Fig. 4, and Fig. S6 and Table S4 in the ESM) [39, 43, 44]. We compared the adsorption behavior of PhSeSePh on metallic Ru and $RuO_2$ surfaces. When a PhSeSePh molecule is placed about 3 Å above the Ru surface and allowed to find a local energy minimum using the conjugate gradient method, an adsorbed configuration with a greatly elongated Se–Se distance is obtained (3.9 Å, much larger than the sum of the van der Waals radii of two Se atoms). Furthermore, the formation of two isolated adsorbed PhSe* species is exothermic, with $\Delta E$ = –0.37 eV. These results imply that the cleavage of the Se–Se bond of PhSeSePh is fairly easy on the metallic Ru surface. In contrast, when a PhSeSePh molecule is adsorbed on the $RuO_2$ surface, the Se–Se distance increases by only 0.2 Å, indicating a limited activating effect of the above surface on the Se–Se bond. Further cleavage of the Se–Se bond on the $RuO_2$ surface is endothermic, with $\Delta E$ = +0.48 eV, suggesting that PhSeSePh molecules are difficult to split into two PhSe* species on the $RuO_2$ surface. The Bader charges on the Se atoms of PhSe* species adsorbed on metallic Ru and $RuO_2$ surfaces were calculated as –0.12*e* and +0.57*e*, respectively. The electron-rich Se atom in PhSe* on the Ru surface is hard to react with nucleophiles, while the corresponding electron-poor Se atom on the $RuO_2$ surface is easily attacked by nucleophiles to

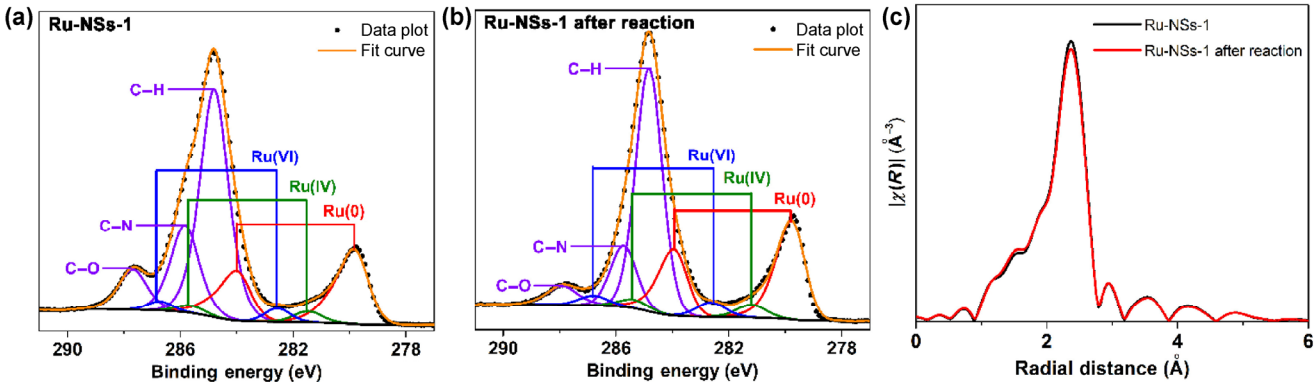


**Figure 2** Ru 3d and C 1s XPS spectra of Ru-NSs-1 before (a) and after the catalytic reaction (b). These spectra were deconvoluted into three C 1s peaks (violet curves) at 284.80, 285.80, and 287.63 eV, assigned to the C atoms in C–H, C–N, and C=O moieties, respectively, and into Ru 3d doublets ($3d_{5/2}$ and $3d_{3/2}$, $\Delta$ = 4.17 eV) with Ru $3d_{5/2}$ binding energies of 279.5–279.9, 281.2–281.4, and 282.6–282.8 eV, assigned to Ru(0) (red curves), Ru(IV) (green curves), and Ru(VI) (blue curves) states, respectively. The results of fitting Ru 3d spectra, which are similar to that of the as-synthesized sample, are shown in Table S3 (in the ESM). Due to the desorption of ligand molecules from the surface of Ru nanospheres, the Ru XPS signals after the catalytic reaction were slightly stronger than those of the as-synthesized sample. (c) R-space Ru K-edge EXAFS spectra of Ru-NSs-1 before and after the reaction.

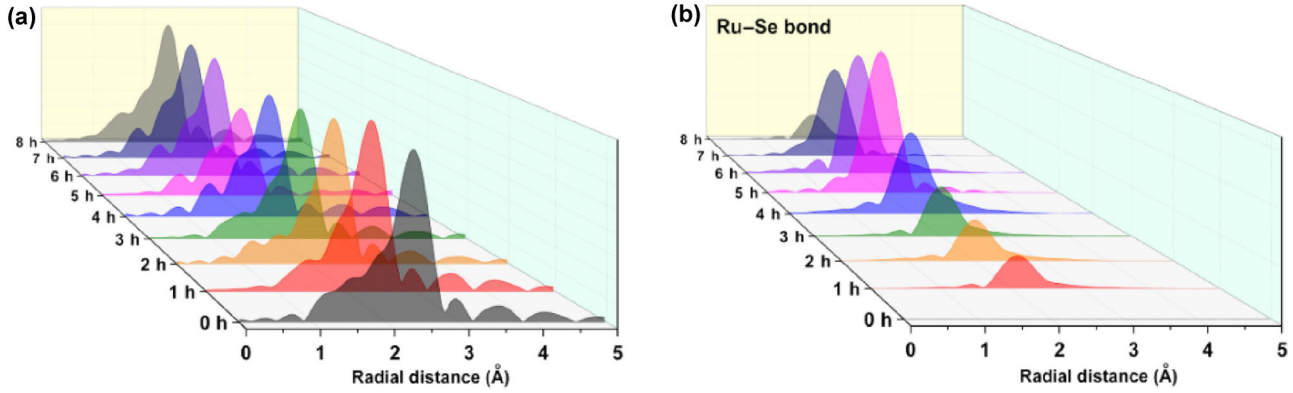


**Figure 3** Ru K-edge *in situ* X-ray adsorption spectroscopy monitoring of (a) Ru-NSs-1 and (b) Ru–Se scattering [26]. The spectra were recorded before the reaction and at reaction times of 0 to 10 h. These peaks were not phase-corrected. The coordination number and interatomic distance data are listed in Table S4 (in the ESM).

form the coupling product. Therefore, neither $RuO_2$ nor metallic Ru are good catalysts for the coupling reaction: $RuO_2$ lacks the capability to break the Se–Se bond, while nucleophilic attack cannot occur on the metallic Ru surface. If metallic Ru and $RuO_2$ surfaces can be combined in one Ru-$RuO_x$ nanoparticle for synergistic catalysis [45–52], a PhSeSePh molecule can be initially adsorbed and cleaved into two PhSe* species on metallic Ru sites, subsequently migrating to $RuO_2$ sites and reacting with the nucleophile (Het = heterocycles)

$$(Ru^0)_{surf} + 0.5PhSeSePh \rightarrow (Ru^0)_{surf} - *SePh$$

$$(Ru^0)_{surf} - *SePh + (Ru^{n+})_{surf} \rightarrow (Ru^{n+})_{surf} - *SePh + (Ru^0)_{surf}$$

$$(Ru^{n+})_{surf} - *SePh + Het \rightarrow (Ru^{n+})_{surf} + Het - SePh$$

According to this synergistic effect, the optimized catalyst should maximize the connection between metallic Ru and $RuO_2$ sites, which can be realized only for Ru-$RuO_x$ nanocatalysts with an appropriate content of metallic and oxidized Ru, which is related to the Ru(0)/$RuO_x$ ratio of NSs. In order to screen the nanocatalysts, the as-synthesized Ru-NSs-1 were post-reduced by hydrogen under hydrothermal conditions for 1, 4, and 12 h (denoted as Ru-NSs-2, Ru-NSs-3, and Ru-NSs-4), and post-oxidized by oxygen for 1 and 4 h, denoted as Ru-NSs-5 and Ru-NSs-6, respectively (Figs. S1 and S2 in the ESM). The

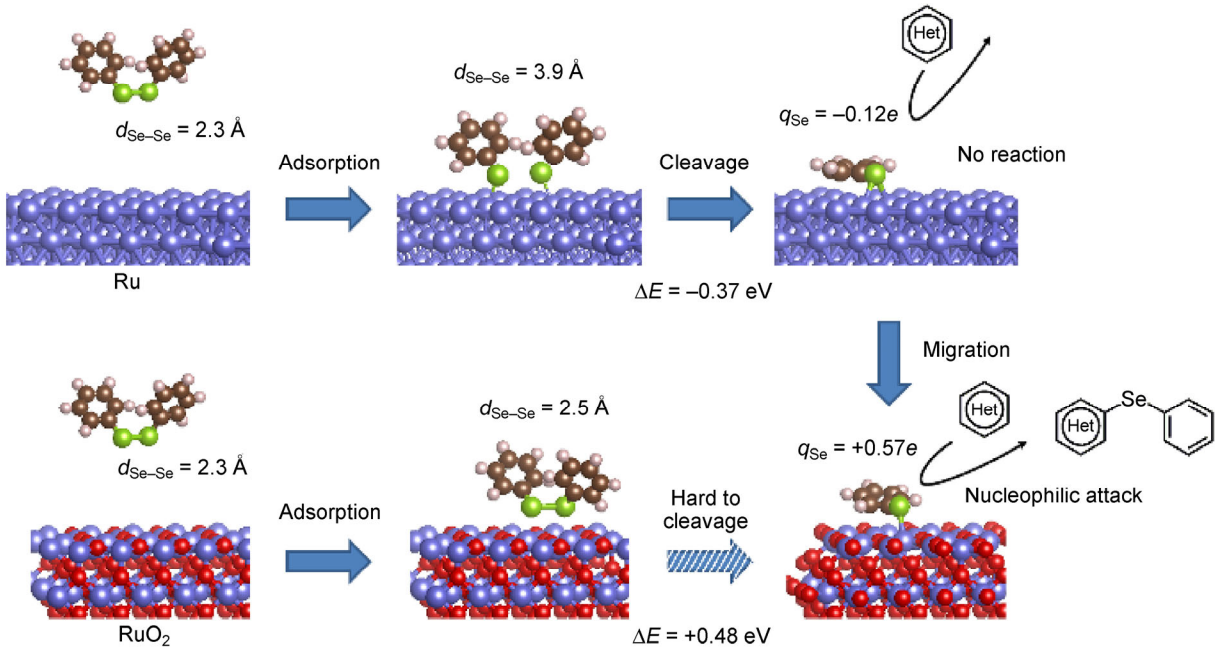


**Figure 4** DFT study and proposed mechanism for the adsorption of PhSeSePh, cleavage of the Se–Se bond, and the nucleophilic attack on the Ru (0001) and $RuO_2$ (110) facets.

contents of Ru with different oxidation states were integrated based on their XPS peaks, showing that the surface oxidation levels of different Ru NSs were in the order of Ru-NSs-6 > Ru-NSs-5 > Ru-NSs-1 > Ru-NSs-2 > Ru-NSs-3 > Ru-NSs-4 (Fig. 5 and Table 1). All these Ru NSs contained metallic and oxidized Ru nanoparticles. Since the diameters of all Ru NSs were quite small (average value of 3.1 ± 0.3 nm), XPS could detect most of the Ru atoms in the sample. Besides, XAFS analysis was also employed to quantify the same oxidation level trend for the whole nanoparticles (Fig. 6 and Fig. S4 in the ESM).

Table 2 shows the apparent turnover frequencies (TOFs) of different Ru NSs, defined as the average number of reagent molecules consumed on one surface Ru site per hour (see the ESM for the calculation process). Different Ru nanocatalysts exhibited different catalytic activities under the same ambient conditions (room temperature, $CH_2Cl_2/CH_3OH$ as solvent, open flask, and absence of energy supplement). In Fig. 7, the TOF values of all Ru catalysts are plotted against their Ru(0)/$RuO_x$ ratio, and the obtained volcano-shaped relationship indicates that Ru NSs with an appropriate balance of metallic and oxidized Ru achieved the highest catalytic activity for the Se–Se activation and selenylation of indole, which further confirms the synergistic effect of Ru and $RuO_x$ in the nanocatalysts.

The control experiments in Table 3 were performed to further confirm the synergistic effect of Ru and $RuO_x$ in the nanocatalysts for the Se–Se bond activation and selenylation of heterocycles. In agreement with DFT calculations, neither Ru/C nor Ru powder or $RuO_2$ exhibited catalytic activity in the Se–Se activation reaction (entries 3–5), with their physical mixture also being inactive (entry 7). When 4 mol.% of Ru-NSs-4 with the highest Ru(0)/$RuO_x$ ratio and 4 mol.% of Ru-NSs-6 with the lowest Ru(0)/$RuO_x$ ratio were added to catalyze this reaction, the obtained TOF was only 0.01 $h^{-1}$, corresponding to low catalytic activity (entry 8). More interestingly, the TOF of the model reaction homogeneously catalyzed by $RuCl_3$ (entry 3) is only 0.08 $h^{-1}$, which is lower than most values obtained for heterogeneous catalysis. All these results confirmed the synergistic effect from another aspect, with the active sites represented by both the low-valence-state metallic Ru and the high-valence-state $RuO_x$ on one Ru-$RuO_x$ nanoparticle, rather than by Ru ions with an intermediate valence state.

We further explored the generality of this reaction

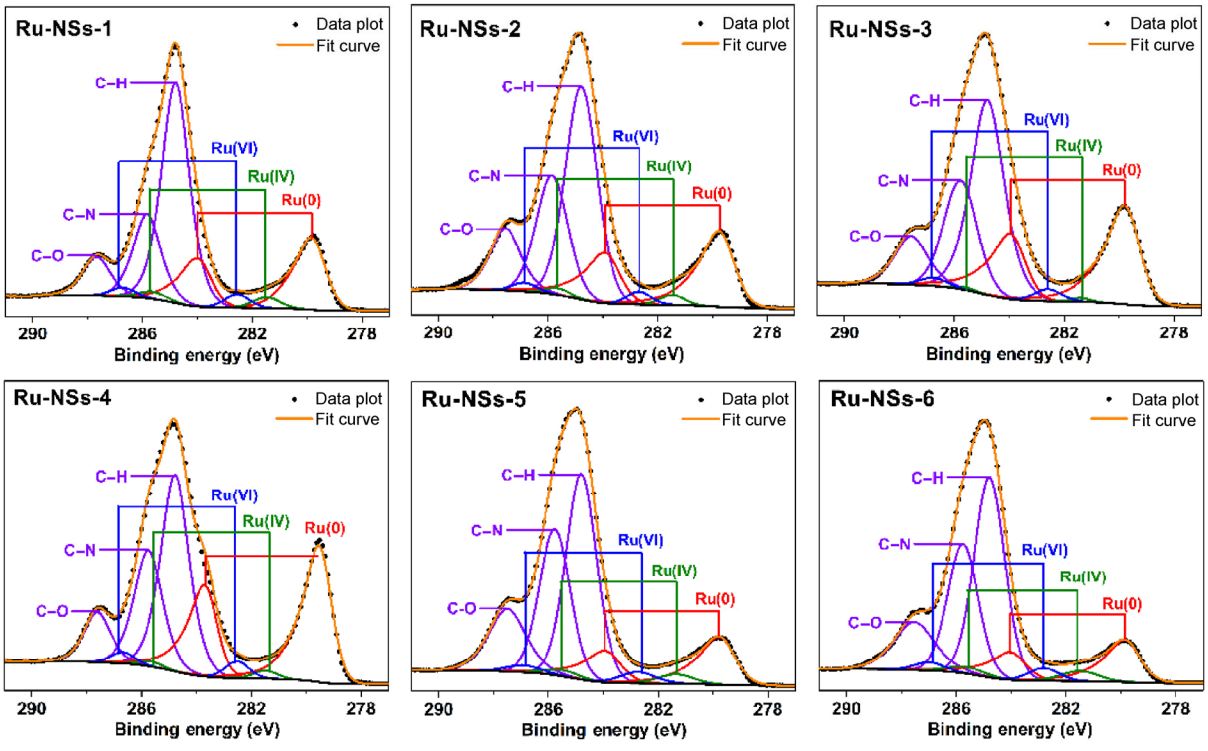


**Figure 5** XPS spectra of all the catalysts in Ru 3d region.

**Table 1** The results of Ru 3d XPS data fitting for all catalysts

| Sample | Ru(0) | | Ru(IV) | | Ru(VI) | | Ru(0):$RuO_x$ |
|---|---|---|---|---|---|---|---|
| | B. E. [a] (eV) | Ratio (%) | B. E. (eV) | Ratio (%) | B. E. (eV) | Ratio (%) | |
| Ru-NSs-1 | 279.8 | 76.2 | 281.3 | 11.3 | 282.6 | 12.5 | 3.20 |
| Ru-NSs-2 | 279.8 | 78.0 | 281.4 | 9.6 | 282.7 | 12.4 | 3.55 |
| Ru-NSs-3 | 279.8 | 82.5 | 281.4 | 5.8 | 282.6 | 11.7 | 4.71 |
| Ru-NSs-4 | 279.8 | 85.1 | 281.5 | 4.7 | 282.6 | 10.2 | 5.71 |
| Ru-NSs-5 | 279.8 | 67.9 | 281.4 | 14.8 | 282.8 | 17.4 | 2.12 |
| Ru-NSs-6 | 279.8 | 62.8 | 281.4 | 18.8 | 282.8 | 18.7 | 1.69 |
| Ru-NSs-1 after reaction | 279.8 | 76.4 | 281.2 | 11.0 | 282.6 | 12.6 | 3.24 |

[a] B. E., Ru $3d_{5/2}$ binding energy.

under the standard conditions. To our satisfaction, the reaction proceeded well, resulting in Se–Se bond activation for the selenylation of heterocycles (Table 4).

## 4 Conclusions

Hydrothermally synthesized Ru NSs were used for Se–Se bond activation. Compared to homogeneous catalysis, this new procedure for the selenylation of heterocycles is effective, free of energy supplements, and scalable to gram-scale production. We demonstrated that this superior activity can be attributed to the synergistic effect of Ru and $RuO_x$ in the nanoparticles. A further DFT study aimed at understanding the synergistic catalysis by Ru-$RuO_x$ nanoparticles suggested that a PhSeSePh molecule can initially be adsorbed on metallic Ru sites and cleaved into two PhSe* species, which then migrate to $RuO_2$ sites and react with the nucleophile to achieve the selenylation of heterocycles. Therefore, this synergistic effect

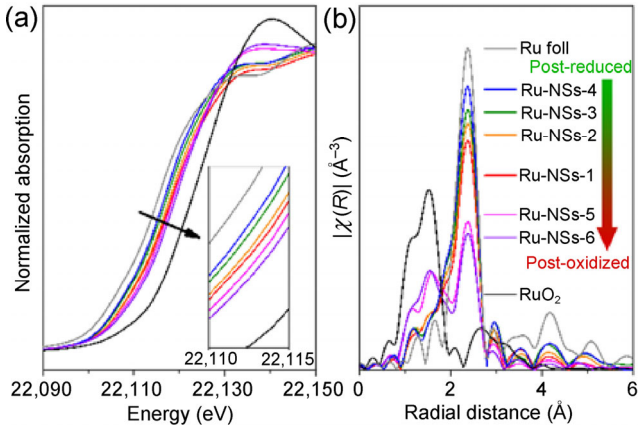


**Figure 6** Ru K-edge (a) X-ray absorption near edge structure (XANES) spectra and (b) R-space EXAFS spectra for Ru foil (gray, 1/2 intensity), Ru-NSs-1 (red), Ru-NSs-2 (orange), Ru-NSs-3 (green), Ru-NSs-4 (blue), Ru-NSs-5 (pink), Ru-NSs-6 (violet), and $RuO_2$ (black). The higher Ru K-edge energy in the XANES spectra reflects the higher Ru oxidation level, which is consistent with the EXAFS data. The FT of $k^2$-weighted extended EXAFS data shows two main peaks around 2.0 and 2.7 Å, attributed to Ru–O and Ru–Ru scattering [38], respectively. The intensity ratio of these peaks reflected the order of oxidation levels, showing a trend identical to that obtained by XANES.

**Table 2** Parameters of the catalytic reactions with different Ru catalysts

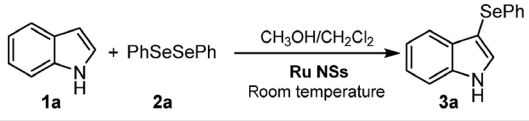


| Entry | Catalyst | Solvent | Yield[a] (%) | TOF[b] ($h^{-1}$) |
|---|---|---|---|---|
| 1 | Ru-NSs-1 | $CH_3OH/CH_2Cl_2$ | 99 | 0.27 |
| 2 | Ru-NSs-1 | $EtOH/CH_2Cl_2$ | 95 | 1.78[c] |
| Ru-NSs-1 post-reduced by $H_2$ | | | | |
| 3 | Ru-NSs-2 | $CH_3OH/CH_2Cl_2$ | 90 | 0.32 |
| 4 | Ru-NSs-3 | $CH_3OH/CH_2Cl_2$ | 96 | 1.58 |
| 5 | Ru-NSs-3 | $EtOH/CH_2Cl_2$ | 97 | 9.57[c] |
| 6 | Ru-NSs-4 | $CH_3OH/CH_2Cl_2$ | 12 | 0.17 |
| Ru-NSs-1 post-oxidized by $O_2$ | | | | |
| 7 | Ru-NSs-5 | $CH_3OH/CH_2Cl_2$ | 86 | 0.04 |
| 8 | Ru-NSs-6 | $CH_3OH/CH_2Cl_2$ | Trace | 0.01 |

[a]8 mol.% of Ru-NSs-1, 0.10 mmol of **1a**, 2 equiv. of **2a**, 0.1 M concentration. Isolated yield after column chromatography. [b]The TOF was obtained for the conversion of substrate **1a** below 15%. The methods used to calculate the number of catalytic sites are shown in the ESM. [c]Reaction temperature equals 70 °C.

results in a volcano-shaped relationship between the content of metallic and oxidized Ru in NSs and their catalytic activities, leading to the rational design, optimization, and synthesis of nanomaterials with high catalytic activities. In this context, we have not only studied the underlying principles and the associated dominant factors of nanocatalysis for the development of efficient and versatile approaches to heterogeneous catalysis under ambient conditions, but also offered new and valuable mechanistic insights into inorganic nanocatalysts and organic methodologies.

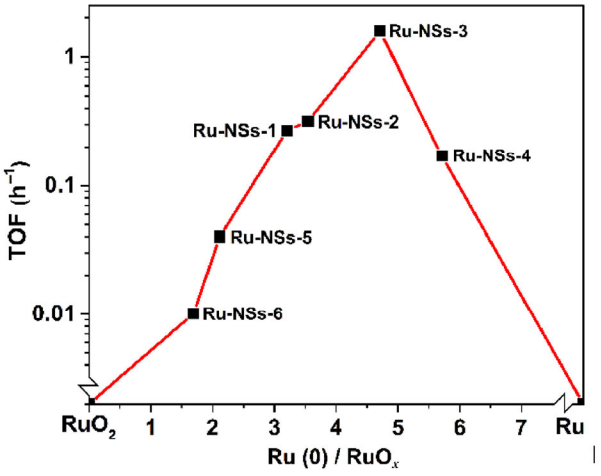


**Figure 7** Plots of Ru NS catalyst TOFs against the surface $Ru(0)/RuO_x$ ratio calculated from Ru 3d XPS spectra.

**Table 3** Control experiments

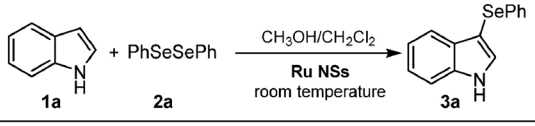


| Entry | Catalyst | Solvent | Yield[a] (%) | TOF[b] ($h^{-1}$) |
|---|---|---|---|---|
| 1 | Ru-NSs-1 | $CH_3OH/CH_2Cl_2$ | 99 | 0.27 |
| 2 | Ru-NSs-1 | $EtOH/CH_2Cl_2$ | 95 | 1.78[c] |
| 3 | Ru/C | $CH_3OH/CH_2Cl_2$ | No reaction | — |
| 4 | Ru powder | $CH_3OH/CH_2Cl_2$ | No reaction | — |
| 5 | $RuO_2$ | $CH_3OH/CH_2Cl_2$ | No reaction | — |
| 6 | $RuCl_3$ | $CH_3OH/CH_2Cl_2$ | 65 | 0.08 |
| 7 | Ru powder + $RuO_2$ | $CH_3OH/CH_2Cl_2$ | No reaction | —[d] |
| 8 | Ru-NSs-4 + Ru-NSs-6 | $CH_3OH/CH_2Cl_2$ | 7 | 0.01[d] |

[a]8 mol.% of Ru-NSs-1, 0.10 mmol of **1a**, 2 equiv. of **2a**, 0.1 M concentration. Isolated yield after column chromatography. [b]The TOF was obtained for a conversion of substrate **1a** below 15%. The methods used to calculate the number of catalytic sites are shown in the ESM. [c]Reaction temperature equals 70 °C. [d]4 mol.% of Ru powder and 4 mol.% of $RuO_2$, 4 mol.% of Ru-NSs-4 and 4 mol.% of Ru-NSs-6.

**Table 4** Se–Se bond activation for selenylation catalyzed by Ru nanocomposites [a]

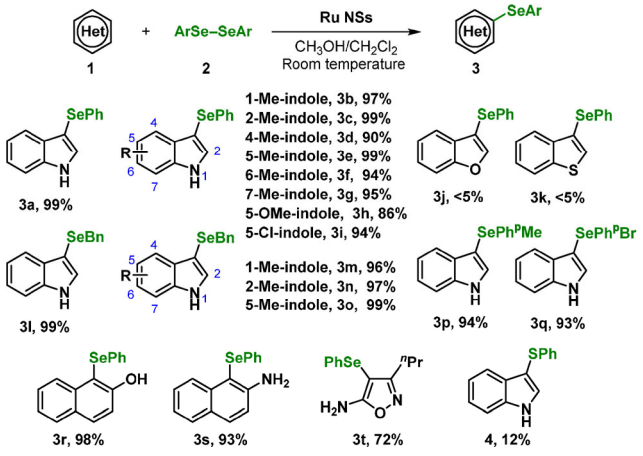


[a]Reaction conditions: 8 mol.% Ru-NSs-1, 0.10 mmol of **1a**, 2 equiv. of **2a**, 0.1 M concentration. Isolated yield after column chromatography.

## Acknowledgements

We thank the National Natural Science Foundation of China (Nos. 21461162001, 21025101, 21371011, 21321001, 21229101, and 21331001), the National Basic Research Program of China (No. 2012CBA01204) for financial support, and the 7th China Postdoctoral Science Foundation Funded Project (No. 2014T70009). M. L. was also supported in part by the Postdoctoral Fellowship of Peking-Tsinghua Center for Life Sciences.

**Electronic Supplementary Material**: Supplementary material (synthesis, characterization, catalysis study of Ru nanospheres, and further details of organic experiments) is available in the online version of this article at http://dx.doi.org/10.1007/s12274-016-1350-0.

## References

[1] Schlögl, R.; Hamid, S. B. A. Nanocatalysis: Mature science revisited or something really new? *Angew. Chem., Int. Ed.* **2004**, *43*, 1628–1637.

[2] Astruc, D.; Lu, F.; Aranzaes, J. R. Nanoparticles as recyclable catalysts: The frontier between homogeneous and heterogeneous catalysis. *Angew. Chem., Int. Ed.* **2005**, *44*, 7852–7872.

[3] Wang, D. S.; Xie, T.; Li, Y. D. Nanocrystals: Solution-based synthesis and applications as nanocatalysts. *Nano Res.* **2009**, *2*, 30–46.

[4] Lee, I.; Delbecq, F.; Morales, R.; Albiter, M. A.; Zaera, F. Tuning selectivity in catalysis by controlling particle shape. *Nat. Mater.* **2009**, *8*, 132–138.

[5] Polshettiwar, V.; Varma, R. S. Green chemistry by nano-catalysis. *Green Chem.* **2010**, *12*, 743–754.

[6] Zahmakıran, M.; Özkar, S. Metal nanoparticles in liquid phase catalysis; from recent advances to future goals. *Nanoscale* **2011**, *3*, 3462–3481.

[7] Chng, L. L.; Erathodiyil, N.; Ying, J. Y. Nanostructured catalysts for organic transformations. *Acc. Chem. Res.* **2013**, *46*, 1825–1837.

[8] Li, Z.-X.; Xue, W.; Guan, B.-T.; Shi, F.-B.; Shi, Z.-J.; Jiang, H.; Yan, C.-H. A conceptual translation of homogeneous catalysis into heterogeneous catalysis: Homogeneous-like heterogeneous gold nanoparticle catalyst induced by ceria supporter. *Nanoscale* **2013**, *5*, 1213–1220.

[9] Jiang, B. J.; Song, S. Z.; Wang, J. Q.; Xie, Y.; Chu, W. Y.; Li, H. F.; Xu, H.; Tian, C. G.; Fu, H. G. Nitrogen-doped graphene supported Pd@PdO core–shell clusters for C–C coupling reactions. *Nano Res.* **2014**, *7*, 1280–1290.

[10] Wang, S.-B.; Zhu, W.; Ke, J.; Lin, M.; Zhang, Y.-W. Pd-Rh nanocrystals with tunable morphologies and compositions as efficient catalysts toward Suzuki cross-coupling reactions. *ACS Catal.* **2014**, *4*, 2298–2306.

[11] Wang, F.; Li, C.; Chen, H.; Jiang, R.; Sun, L.-D.; Li, Q.; Wang, J.; Yu, J. C.; Yan, C.-H. Plasmonic harvesting of light energy for Suzuki coupling reactions. *J. Am. Chem. Soc.* **2013**, *135*, 5588–5601.

[12] Wu, Y. E.; Li, Y. D. New understanding of phase segregation of bimetallic nanoalloys. *Sci. China Mater.* **2015**, *58*, 3–4.

[13] Dai, L.-X.; Zhu, W.; Lin, M.; Zhang, Z.-P.; Gun, J.; Wang, Y.-H.; Zhang, Y.-W. Self-supported composites of thin Pt–Sn crosslinked nanowires for the highly chemoselective hydrogenation of cinnamaldehyde under ambient conditions. *Inorg. Chem. Front.* **2015**, *2*, 949–956.

[14] Xiao, B.; Niu, Z. Q.; Wang, Y.-G.; Jia, W.; Shang, J.; Zhang, L.; Wang, D. S.; Fu, Y.; Zeng, J.; He, W. et al. Copper nanocrystal plane effect on stereoselectivity of catalytic deoxygenation of aromatic epoxides. *J. Am. Chem. Soc.* **2015**, *137*, 3791–3794.

[15] Guo, H. F.; Yan, X. L.; Zhi, Y.; Li, Z. W.; Wu, C.; Zhao, C. L.; Wang, J.; Yu, Z. X.; Ding, Y.; He, W. et al. Nanostructuring gold wires as highly durable nanocatalysts for selective reduction of nitro compounds and azides with organosilanes. *Nano Res.* **2015**, *8*, 1365–1372.

[16] Chen, Y. G.; Yu, Z. J.; Chen, Z.; Shen, R. A.; Wang, Y.; Gao, X.; Peng, Q.; Li, Y. D. Controlled one-pot synthesis of RuCu nanocages and Cu@Ru nanocrystals for the regioselective hydrogenation of quinoline. *Nano Res.* **2016**, *9*, 2632–2640.

[17] Gong, M.; Wang, D.-Y.; Chen, C.-C.; Hwang, B.-J.; Dai, H. J. A mini review on nickel-based electrocatalysts for alkaline hydrogen evolution reaction. *Nano Res.* **2016**, *9*, 28–46.

[18] Zhang, Z.-P.; Wang, X.-Y.; Yuan, K.; Zhu, W.; Zhang, T.; Wang, Y.-H.; Ke, J.; Zheng, X.-Y.; Yan, C.-H.; Zhang, Y.-W. Free-standing iridium and rhodium-based hierarchically-coiled ultrathin nanosheets for highly selective reduction of nitrobenzene to azoxybenzene under ambient conditions. *Nanoscale* **2016**, *8*, 15744–15752.

[19] Casini, A.; Winum, J. Y.; Montero, J. L.; Scozzafava, A.; Supuran, C. T. Carbonic anhydrase inhibitors: Inhibition of cytosolic isozymes I and II with sulfamide derivatives. *Bioorg. Med. Chem. Lett.* **2003**, *13*, 837–840.

[20] Mellah, M.; Voituriez, A.; Schulz, E. Chiral sulfur ligands for asymmetric catalysis. *Chem. Rev.* **2007**, *107*, 5133–5209.

[21] Murphy, A. R.; Fréchet, J. M. J. Organic semiconducting oligomers for use in thin film transistors. *Chem. Rev.* **2007**, *107*, 1066–1096.

[22] Sato, T.; Nishio, M.; Ishii, Y.; Yamazaki, H.; Hidai, M. Synthesis and reactivities of the indenyl-ruthenium cluster $[(\eta^5\text{-}C_9H_7)Ru(\mu\text{-}SEt)]_3$: Indenyl effect in the trinuclear ruthenium cluster. *J. Organomet. Chem.* **1998**, *569*, 99–108.

[23] Belletti, D.; Graiff, C.; Lostao, V.; Pattacini, R.; Predieri, G.; Tiripicchio, A. Sulfido–carbonyl ruthenium clusters derived from tertiary phosphine sulfides. *Inorg. Chim. Acta* **2003**, *347*, 137–144.

[24] Becker, E.; Mereiter, K.; Schmid, R.; Kirchner, K. Facile S−S bond activation of alkyl and aryl disulfides by $[RuCp(CH_3CN)_3]^+$: Formation of dinuclear Ru(III)−Ru(III) complexes with bridging thiolate ligands. *Organometallics* **2004**, *23*, 2876–2883.

[25] Maiti, B. K.; Görls, H.; Klobes, O.; Imhof, W. A straightforward and generalizable synthetic methodology for the synthesis of ruthenium(II) complexes with thioether ligands from either Ru(III) or Ru(0) precursors. *Dalton Trans.* **2010**, *39*, 5713–5720.

[26] Begum, N.; Hyder, M. I.; Hassan, M. R.; Kabir, S. E.; Bennett, D. W.; Haworth, D. T.; Siddiquee, T. A.; Rokhsana, D.; Sharmin, A.; Rosenberg, E. Facile E−E and E−C bond activation of PhEEPh (E = Te, Se, S) by ruthenium carbonyl clusters: Formation of di- and triruthenium complexes bearing bridging dppm and phenylchalcogenide and capping chalcogenido ligands. *Organometallics* **2008**, *27*, 1550–1560.

[27] Nagarajaprakash, R.; Ramakrishna, B.; Mahesh, K.; Mobin, S. M.; Manimaran, B. One-pot synthesis of ruthenium metallacycles via oxidative addition of diaryldichalcogen and halogen across a Ru–Ru bond. *Organometallics* **2013**, *32*, 7292–7296.

[28] Horiuchi, S.; Murasem, T.; Fujita, M. Noncovalent trapping and stabilization of dinuclear ruthenium complexes within a coordination cage. *J. Am. Chem. Soc.* **2011**, *133*, 12445–12447.

[29] Yao, S. A.; Martin-Diaconescu, V.; Infante, I.; Lancaster, K. M.; Götz, A. W.; DeBeer, S.; Berry, J. F. Electronic structure of $Ni_2E_2$ complexes (E = S, Se, Te) and a global analysis of $M_2E_2$ compounds: A case for quantized $E_2^{n-}$ oxidation levels with $n$ = 2, 3, or 4. *J. Am. Chem. Soc.* **2015**, *137*, 4993–5011.

[30] Aufieco, M.; Sperger, T.; Tsang, A. S.-K.; Schoenebeck, F. Highly efficient C−$SeCF_3$ coupling of aryl iodides enabled by an air-stable dinuclear $Pd^I$ catalyst. *Angew. Chem., Int. Ed.* **2015**, *54*, 10322–10326.

[31] Yin, A. X.; Liu, W.-C.; Ke, J.; Zhu, W.; Gu, J.; Zhang, Y.-W.; Yan, C.-H. Ru nanocrystals with shape-dependent surface-enhanced Raman spectra and catalytic properties: Controlled synthesis and DFT calculations. *J. Am. Chem. Soc.* **2012**, *134*, 20479–20489.

[32] Sang, P.; Chen, Z. K.; Zou, J. W.; Zhang, Y. H. $K_2CO_3$ promoted direct sulfenylation of indoles: A facile approach towards 3-sulfenylindoles. *Green Chem.* **2013**, *15*, 2096–2100.

[33] Azeredo, J. B.; Godoi, M.; Martins, G. M.; Silveira, C. C.; Braga, A. L. A solvent- and metal-free synthesis of 3-chacogenyl-indoles employing DMSO/$I_2$ as an eco-friendly catalytic oxidation system. *J. Org. Chem.* **2014**, *79*, 4125–4130.

[34] Vásquez-Céspedes, S.; Ferry, A.; Candish, L.; Glorius, F. Heterogeneously catalyzed direct C−H thiolation of heteroarenes. *Angew. Chem., Int. Ed.* **2015**, *54*, 5772–5776.

[35] Ferreira, N. L.; Azeredo, J. B.; Fiorentin, B. L.; Braga, A. L. Synthesis of 3-selenylindoles under ecofriendly conditions. *Eur. J. Org. Chem.* **2015**, *23*, 5070–5074.

[36] Lewera, A.; Zhou, W. P.; Vericat, C.; Chung, J. H.; Haasch, R.; Wieckowski, A.; Bagus, P. S. XPS and reactivity study of bimetallic nanoparticles containing Ru and Pt supported on a gold disk. *Electrochim. Acta* **2006**, *51*, 3950–3956.

[37] Mazzieri, V.; Coloma-Pascual, F.; Arcoya, A.; L'Argentière, P. C.; Figoli, N. S. XPS, FTIR and TPR characterization of $Ru/Al_2O_3$ catalysts. *Appl. Surf. Sci.* **2003**, *210*, 222–230.

[38] Mitsudome, T.; Takahashi, Y.; Mizugaki, T.; Jitsukawa, K.; Kaneda, K. Hydrogenation of sulfoxides to sulfides under mild conditions using ruthenium nanoparticle catalysts. *Angew. Chem., Int. Ed.* **2014**, *53*, 8348–8351.

[39] Vogel, W.; Kaghazchi, P.; Jacob, T.; Alonso-Vante, N. Genesis of $Ru_xSe_y$ nanoparticles by pyrolysis of $Ru_4Se_2(CO)_{11}$: A combined X-ray *in situ* and DFT study. *J. Phys. Chem. C* **2007**, *111*, 3908–3913.

[40] Inukai, J.; Cao, D. X.; Wieckowski, A.; Chang, K.-C.; Menzel, A.; Komanicky, V.; You, H. *In situ* synchrotron

X-ray spectroscopy of ruthenium nanoparticles modified with selenium for an oxygen reduction reaction. *J. Phys. Chem. C* **2007**, *111*, 16889–16894.

[41] Haas, S.; Zehl, G.; Dorbandt, I.; Manke, I.; Bogdanoff, P.; Fiechter, S.; Hoell, A. Direct accessing the nanostructure of carbon supported Ru−Se based catalysts by ASAXS. *J. Phys. Chem. C* **2010**, *114*, 22375–22384.

[42] Ramaswamy, N.; Allen, R. J.; Mukerjee, S. Electrochemical kinetics and X-ray absorption spectroscopic investigations of oxygen reduction on chalcogen-modified ruthenium catalysts in alkaline media. *J. Phys. Chem. C* **2011**, *115*, 12650–12664.

[43] Cánaves, M. M.; Cabra, M. I.; Bauzá, A.; Cañellas, P.; Sánchez, K.; Orvay, F.; García-Raso, A.; Fiol, J. J.; Terrón, A.; Barceló-Oliver, M. et al. Crystal structures and DFT calculations of new chlorido-dimethylsulfoxide-M(III) (M = Ir, Ru, Rh) complexes with the N-pyrazolyl pyrimidine donor ligand: Kinetic vs. thermodynamic isomers. *Dalton Trans.* **2014**, *43*, 6353–6364.

[44] Gu, J.; Guo, Y.; Jiang, Y.-Y.; Zhu, W.; Xu, Y.-S.; Zhao, Z.-Q.; Liu, J.-X.; Li, W.-X.; Jin, C.-H.; Yan, C.-H. et al. Robust phase control through hetero-seeded epitaxial growth for face-centered cubic Pt@Ru nanotetrahedrons with superior hydrogen electro-oxidation activity. *J. Phys. Chem. C* **2015**, *119*, 17697–17706.

[45] Liang, J.; Jiao, Y.; Jaroniec, M.; Qiao, S. Z. Sulfur and nitrogen dual-doped mesoporous graphene electrocatalyst for oxygen reduction with synergistically enhanced performance. *Angew. Chem., Int. Ed.* **2012**, *51*, 11496–11500.

[46] Li, L. L.; Chen, X. B.; Wu, Y. E.; Wang, D. S.; Peng, Q.; Zhou, G.; Li, Y. D. Pd-$Cu_2O$ and Ag-$Cu_2O$ hybrid concave nanomaterials for an effective synergistic catalyst. *Angew. Chem., Int. Ed.* **2013**, *52*, 11049–11053.

[47] Zhou, F.; Xin, S.; Liang, H.-W.; Song, L.-T.; Yu, S.-H. Carbon nanofibers decorated with molybdenum disulfide nanosheets: Synergistic lithium storage and enhanced electrochemical performance. *Angew. Chem., Int. Ed.* **2014**, *53*, 11552–11556.

[48] Qadir, K.; Joo, S. H.; Mun, B. S.; Butcher, D. R.; Renzas, J. R.; Aksoy, F.; Liu, Z.; Somorjai, G. A.; Park, J. Y. Intrinsic relation between catalytic activity of CO oxidation on Ru nanoparticles and Ru oxides uncovered with ambient pressure XPS. *Nano Lett.* **2012**, *12*, 5761–5768.

[49] Lettenmeier, P.; Wang, L.; Golla-Schindler, U.; Gazdzicki, P.; Cañas, N. A.; Handl, M.; Hiesgen, R.; Hosseiny, S. S.; Gago, A. S.; Friedrich, K. A. Nanosized $IrO_x$–Ir catalyst with relevant activity for anodes of proton exchange membrane electrolysis produced by a cost-effective procedure. *Angew. Chem., Int. Ed.* **2016**, *55*, 742–746.

[50] Gao, S.; Lin, Y.; Jiao, X. C.; Sun, Y. F.; Luo, Q. Q.; Zhang, W. H.; Li, D. Q.; Yang, J. L.; Xie, Y. Partially oxidized atomic cobalt layers for carbon dioxide electroreduction to liquid fuel. *Nature* **2016**, *529*, 68–71.

[51] Luska, K. L.; Bordet, A.; Tricard, S.; Sinev, I.; Grünert, W.; Chaudret, B.; Leitner, W. Enhancing the catalytic properties of ruthenium nanoparticle-SILP catalysts by dilution with Iron. *ACS Catal.* **2016**, *6*, 3719–3726.

[52] Xiao, C. X.; Goh, T.-W.; Qi, Z. Y.; Goes, S.; Brashler, K.; Perez, C.; Huang, W. Y. Conversion of Levulinic acid to γ-valerolactone over few-layer graphene-supported ruthenium catalysts. *ACS Catal.* **2016**, *6*, 593–599.